INL/RPT-22-69281
Revision 0

Phase II Development of the Surveillance Test Articles to Improve the Design, Fabrication, and Testing

September 2022

Michael McMurtrey, Heramb Mahajan, M. Nedim Cinbiz, Kaelee Novich, Timothy Phero, Thomas Walters, Ting-Leung Sham

Idaho National Laboratory

INL is a U.S. Department of Energy National Laboratory operated by Battelle Energy Alliance, LLC

INL/RPT-22-69281
Revision 0

Phase II Development of the Surveillance Test Articles to Improve the Design, Fabrication, and Testing

Michael McMurtrey, Heramb Mahajan, M. Nedim Cinbiz, Kaelee Novich, Timothy Phero, Thomas Walters, Ting-Leung Sham

September 2022

Idaho National Laboratory
Advanced Reactor Technologies
Idaho Falls, Idaho 83415

http://www.art.inl.gov

Prepared for the
U.S. Department of Energy
Office of Nuclear Energy
Under DOE Idaho Operations Office
Contract DE-AC07-05ID14517

Page intentionally left blank

INL ART Program

Phase II Development of the Surveillance Test Articles to Improve the Design, Fabrication, and Testing

INL/RPT-22-69281
Revision 0
September 2022

Technical Reviewer: (Confirmation of mathematical accuracy, and correctness of data and appropriateness of assumptions.)

ninadmohale — 9/19/2022
Ninad Mohale — Date

Approved by:

M. Davenport — 9/19/2022
Michael E. Davenport — Date
ART Project Manager

Travis Mitchell — 9/20/2022
Travis R. Mitchell — Date
ART Program Manager

Michelle Sharp — 9/20/2022
Michelle T. Sharp — Date
INL Quality Assurance

ACKNOWLEDGMENTS

This research was sponsored by the U.S. Department of Energy (DOE) under Contract No. DE-AC07-05ID14517 with Idaho National Laboratory (INL), which is managed and operated by Battelle Energy Alliance. Programmatic direction was provided by the Office of Nuclear Reactor Deployment of the DOE Office of Nuclear Energy (NE).

The authors gratefully acknowledge the support provided by Sue Lesica of DOE NE, Federal Lead for Advanced Materials, Advanced Reactor Technologies (ART) Program; Brian Robinson, Federal Manager, ART Molten Salt Reactors (MSR) Campaign; and Patricia Paviet, Pacific Northwest National Laboratory, National Technical Director, ART MSR Campaign.

The authors also acknowledge helpful discussions with Mark Messner of the Argonne National Laboratory.

Acronyms

ANL	Argonne National Laboratory
ART	Advanced Reactors Technologies
CSTA	Circular surveillance test article
CTE	Coefficient of thermal expansion
DIC	Digital image correlation
DICe	Digital Image Correlation Engine
EMF	electromagnetic field
FE	Finite element
INL	Idaho National Laboratory
MSR	Molten salt reactor
SS	Stainless Steel
TZM	Titanium -Zirconium-Molybdenum

1. INTRODUCTION

Advanced reactors, such as the molten salt reactor (MSR), require materials that will withstand harsher environments than the materials used for lower temperature water reactors. Materials used in MSR construction need not only withstand elevated temperature, temperature cycling, and neutron radiation, but must be able to withstand the corrosive molten salt environment. Significant materials research has been driven by the materials needs of the MSR due to the harsh environment and the material data requirements to support licensing. Limited operational experience with MSRs has made this challenging work. Information is very limited on materials degradation due to irradiation, molten salt corrosion, elevated temperature, and the resulting fatigue, creep, and creep-fatigue loading during operation. While efforts are underway to better understand the effects of this harsh environment on construction materials, the Advanced Reactors Technologies (ART) Program has been working to develop materials surveillance test articles that could be used in a materials surveillance program and allow for the collection of information on the materials degradation during plant operation and could support timely licensing of these advanced reactors.

The method of application of surveillance programs in nuclear components is described in the ASTM E531 – Standard Practice for Surveillance Testing of High-Temperature Nuclear Component Materials (ASTM, 2013). This was based on light water reactor technologies and originally approved in 1975. The standard covers procedures for periodic specimen testing performed through the service life of the components to assess changes in selected metallic material properties that are caused by neutron irradiation and thermal effects. It provides guidance on how to place surveillance test articles to obtain the desired irradiation conditions and scheduling of test article removal for mechanical properties testing. The standard is being updated by committees to make it more applicable to advanced reactors.

The ART program has developed a test article that can capture the combination effects of stress, temperature, corrosion, and neutron irradiation, which can be used to augment the current test article selection in ASTM E531. Development of this test article began at Argonne National Laboratory (ANL), where a cylindrical test article was developed and thermally cycled within a furnace (Messner et al., 2018; Messner, et. al, 2020; Messner, Sham, 2021a; Messner, et. al., 2021; Messner, et. al., 2022). The passive loading was obtained due to a thermal expansion mismatch in the materials used to construct the test article. This work has continued at Idaho National Laboratory (INL), where additional instrumentation has been explored for characterizing the surveillance test article, as well as more rapid thermal cycling through induction heating to decrease the required time for characterizing the test article design.

2. NEW TEST ARTICLE DESIGN AND ANALYSIS

The initial work on test article design performed at INL was to examine the ANL test article and how it could be modified with different driver materials and to achieve varying stress and deformation time history during the thermal cycling. A longitudinal cross-sectional figure of the surveillance test article is presented in Figure 1a. This test article had circular cross section; hence referred as Circular Surveillance Test Article (CSTA). Red material has lower coefficient of thermal expansion (CTE) compared to blue material. Test specimen geometry uses a standard ASTM cyclic specimen geometry. This test specimen is welded to drivers. The end of casing and drivers are welded as shown in thick black line in Figure 1a. The schematic of an idealized model of this test article for sizing calculation is constructed by replacing the smooth corners of the specimen with a representative rectangular section as shown in Figure 1b. This idealized model assumes perfect welds between casing and driver. Hence, the actual length in schematic model starts at the weld base between the casing and driver as shown in Figure 1b. For driver with higher CTE mismatch, the weld between the test specimen and driver may experience large stresses which may affect the specimen behavior. Larger notch radius is needed to minimize the influence of the thermal stresses due to CTE mismatch at the welds on the specimen stress. This notch radius introduces additional material between driver-specimen-driver assembly, affecting the strain range and elastic follow-up values

of specimen in CSTA. Hence, a four-bar model is used to capture the influence of notched region of CSTA. The schematic of a symmetric half of this idealized four-bar model is presented in Figure 1c with detailed dimensions. Parameter γ_i represents diameter ratios with respect to total diameter of test article, and l_i is length ratios with respect to total length of test article. The subscripts 1, 2, and 3 represents test specimen, driver, and notch radius. Symmetric boundary condition was used on bottom nodes of specimen and casing, and top nodes of driver and casing are glued and free to move.

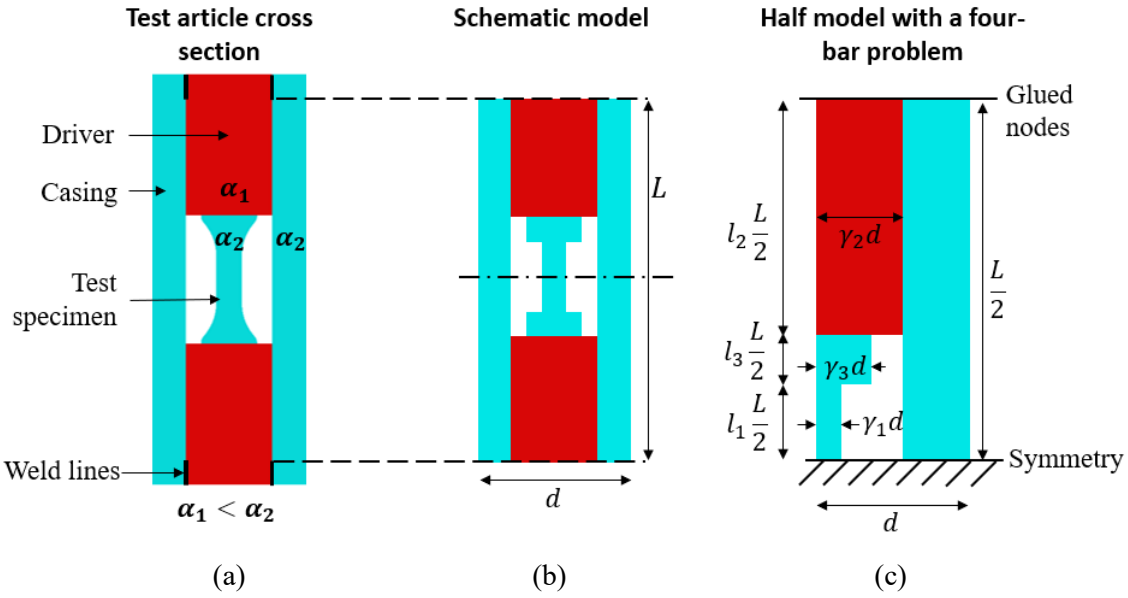

Figure 1. (a) Cross section of the circular surveillance test article, (b) schematic depiction to capture the notch radius, and (c) four-bar representation of the surveillance test article.

The viscoplastic constitutive model available in the Nuclear Engineering Material model Library for stainless steel (SS) 316H was used (Messner and Sham, 2021b). Titanium -Zirconium-Molybdenum alloy (TZM) was selected as a candidate driver material, which has lower CTE compared to previously selected Alloy 617 driver material. The material properties of the TZM were obtained from the literature (Karditsas and Baptiste, 1995). For temperatures up to 700℃ and stresses below the ultimate strength of SS316, TZM remains elastic with negligible accumulation of creep strain. Therefore, an elastic material model was implemented to capture the behavior of TZM in the sizing calculation. The test article temperature was cycled following the temperature load history shown in Figure 2, with peak temperature (T_{max}) of 700℃, temperature difference (ΔT) of 200℃, dwell time (t_{dwell}) of 15 minutes and total cycle time of 30 minutes making ramp up and ramp down time of 7.5 minutes each. The analysis framework developed at ANL (Messner and Sham, 2021a) was used, but with TZM as the driver material for the four-bar problem.

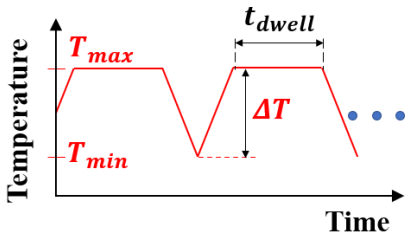

Figure 2. Schematic figure of temperature cycle.

Few cases were simulated, and numerical results are presented in Figure 3. These results show the influence of different parameters on the strain range and elastic follow-up values. The red line indicates cases with changing l_1 parameter with constant γ_1 of 0.36. The black line indicates cases with changing γ_1 parameter with constant l_1 of 0.18. Driver diameter parameter γ_2 is 0.7 and γ_3 is selected such that notch radius region will have average area of driver and test specimen. Increasing l_1 parameter results decrease in elastic follow-up value and strain range. Increasing γ_1 parameter results in an increase in the elastic follow-up value and decrease in the strain range. To achieve the desired strain range and elastic follow-up value, optimization of CSTA geometry is required.

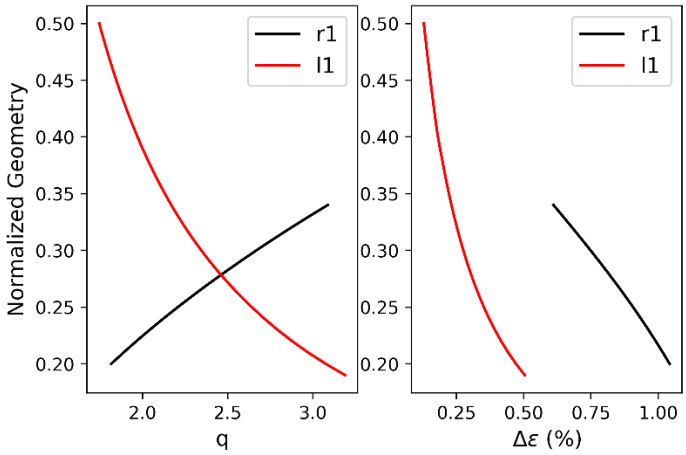

Figure 3. Influence of geometric parameter γ_1 while keeping l_1 constant, and l_1 while keeping γ_1 constant on the strain range and elastic follow-up value.

The four-bar model was optimized with a Genetic Algorithm scheme available in the Python optimization library. This optimization process uses the following constraints for reasons discussed below.

1. $\gamma_2 < 1, l_1 > 0, l_1 < 1$ – These constraints avoid non-physical test article dimensions.
2. $\gamma_1 < \gamma_2$ – This constraint ensures specimen diameter is always smaller than the driver diameter, avoiding the fabrication difficulties and avoid higher stresses at the weld of driver and specimen.
3. $(l_1 L/2)/\phi_1 > 2.1$ – This constraint ensures the length to diameter ratio is always greater than two (2). This is a critical step to achieve uniform stresses in test specimen under cyclic loading at elevated temperatures.
4. $q > 1.1$ and $\Delta\varepsilon < 0.022$ – These constraints avoid geometries that give a small follow-up value and large strain range.

The optimization algorithm provided initial dimensions of the CSTA. These dimensions were used as inputs for a Finite Element (FE) model as shown in Figure 4 to determine the weld stresses. The test article diameter was 25.4 mm (1 inch) and length 101.6 mm (4 inch). The weld between driver-casing and driver-specimen was simulated by gluing nodes on contact surface. The weld length was selected as 6.35 mm (0.25 inch). Temperature cycle history with temperature values discussed above was applied to the test article such that no spatial temperature gradient was allowed. Observation windows were designed on the casing to take pictures to be used for strain measurement in specimen during thermal cycling. The contour maps in Figure 4 shows the peak axial stress distribution at the beginning of dwell time. FE results show the selected weld length should be adequate. Note this analysis assumes perfect weld properties without any defects and does not capture the local material property change due to welding. The hysteresis stress-strain loop obtained in the test specimen shows the strain range of 0.4% and elastic follow-up value of two. This geometry is selected to fabricate and test CSTA.

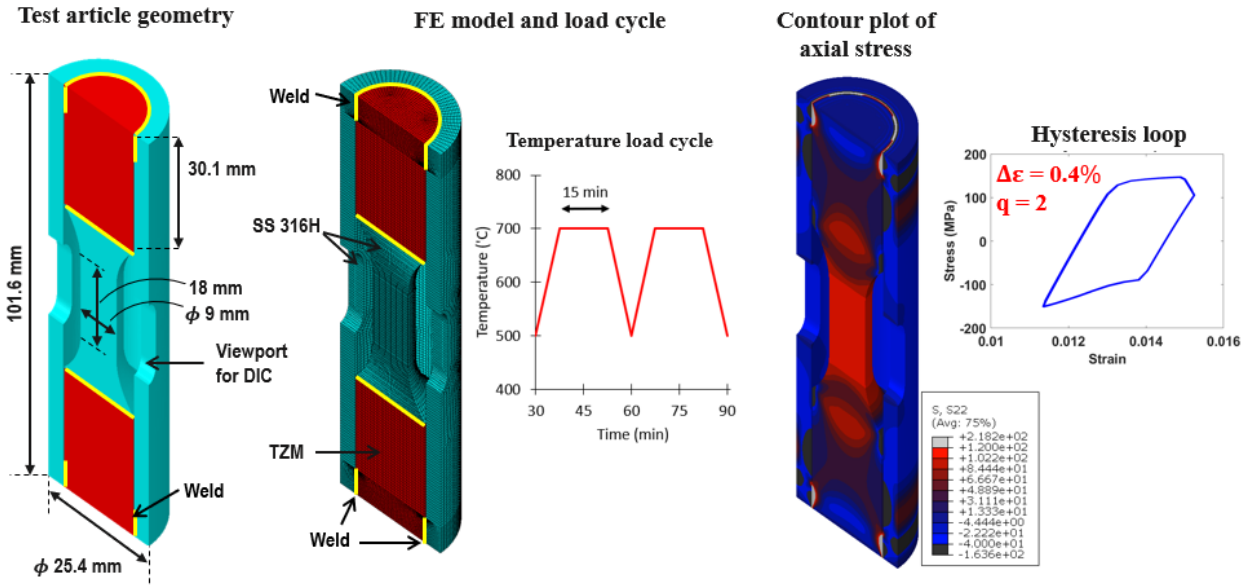

Figure 4. Analysis framework showing the surveillance test article geometry, FE model with temperature cycle applied to the surveillance test article, and results showing the axial stress contour plot with stable hysteresis stress-strain plot in the test specimen.

The CSTA design discussed above has some fabrication issues. Casing and drivers of CSTA are welded through either e-beam welding or laser welding. The welding between casing and driver requires high weld depth, indicating e-beam and laser need to penetrate higher depth of material as shown in Figure 5. Achieving the desired weld depth may not be feasible and the actual weld depth and quality is not easy to inspect. Computed Tomography may be required to assess weld quality, which may not be time and cost efficient. The CSTA results limited access to the gauge length of specimen. The circular section of test article make attaching the strain gauge difficult; limiting the ability to monitor the specimen strain. Although CSTA test articles are smaller compared to the previous proof-of-concept test articles, for small diameter pipes and components these articles may cause fluid flow disruption. The large size of CSTA will result in relatively larger activated volumes, limiting the applicability of CSTA design.

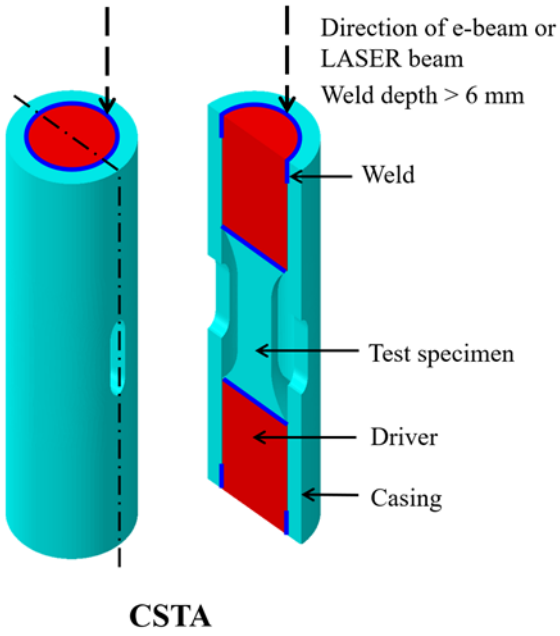

Figure 5. Schematic figure of test article showing weld beam direction for CSTA.

To conduct a driver material comparison of CSTA, a realistic strain range of 0.002 and elastic follow-up of two were selected. CSTA were designed with Alloy 617 and TZM as driver materials. The temperature was cycled from 500℃ to 650℃, with ramp rate of 2.5℃ per minute and dwell time of 100 hours at peak temperature. The four-bar model framework discussed before was used to calculate and compare the dimensions of different drivers. The test article dimensions, and geometry ratios are shownin Table 1.

Table 1. Comparison of CSTA with different driver materials to achieve 0.2% strain range and elastic follow-up of two for peak temperature 650℃, temperature range 150℃, dwell time of 100 hours, ramp up and down in one hour, specimen length of 4 mm, and specimen sectional area of 1.27 mm^2.

	Driver	Diameter/width	Length	γ_1	γ_2	l_1
CSTA	617	8.2	39	0.15488	0.50	0.1026
CSTA	TZM	4.2	17.8	0.30238	0.75	0.2247

These articles were compared in Figure 6, where article sizes are to the scale. As expected, introduction of driver with CTE mismatch results reduction in test article dimensions. Hence, test articles with TZM drivers are smaller compared to articles with Alloy 617 driver. The two CSTA specimens shown in Figure 6 consists of casing thickness of 2.05 mm and 0.525 mm for A617 and TZM driver respectively. CSTA fabrication with such small casing thickness may result in fabrication difficulties. Hence, CSTA specimens need to be scaled up to achieve reasonable casing thickness to avoid fabrication difficulties.

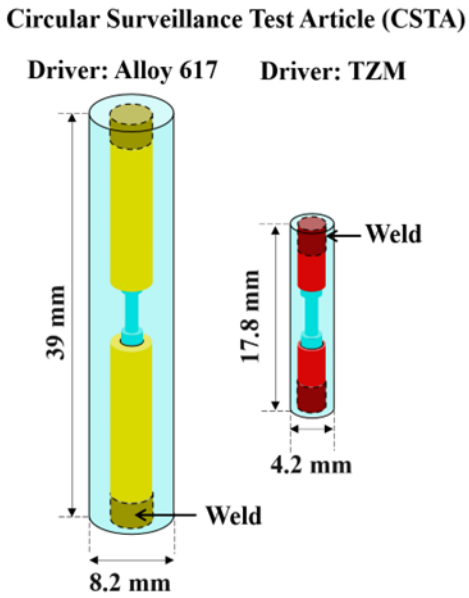

Figure 6. Comparison of the surveillance test article driver materials to achieve 0.2% strain range and elastic follow-up of 2 for peak temperature 650℃, temperature range 150℃, dwell time of 100 hours, ramp up and down in 1 hour, specimen length of 4 mm, and specimen sectional area of 1.27 mm^2

3. NEW EXPERIMENTAL SETUP

The thermal cycling tests at ANL were carried out in a box furnace where the temperature ramp rates are limited due to hardware constraints and there was no line-of-sight of the test article in the box furnace for instrumentation. A new experimental setup has been developed at INL as described in this section to allow for a larger range of temperature ramp rates and additional instrumentation to collect test data.

3.1 Induction Heating

Heating of the surveillance test article will be accomplished with an Ambrell Model 5 (5kW) induction heater and associated Ameritherm chiller for cooling of the induction heating coil and power supply. The heater is capable of being controlled remotely using a 0-10V external signal that scales linearly with the output wattage of the power supply. Ten volts of signal equates to 5kW of output power to the heating coil.

The control and data acquisition system remotely controlling the heater is a National Instruments LabVIEW platform. The hardware side of the platform consists of a cDAQ-9174, 4-slot compact data acquisition chassis. Two of the slots are reserved. One of the slots is occupied with a 0-10V analog voltage output module, NI 9263, and the remaining slot is occupied with a type K thermocouple input module, NI 9162. A Dell Latitude 7400 laptop serves as the host for the control and data acquisition software.

The software side of the platform is National Instruments Base Development system. This software, or virtual instrument customized for these tests, controls the modules - both voltage output and thermocouple measurement. The package is written to continuously scan the temperature of the test article and use it as feed-back for the logic of the control. The voltage output is either 1.51V (approximately 750W) on the ramp-up to temperature, or 0V for the cooling step. Temperature data for various portions of the surveillance test article are logged every 60 seconds to provide the temperature history and profile of the test article during cycling. This control system is currently being set up and tested. Preliminary testing of the induction heating with the CSTA did not use an automated control system. The heater was manually controlled by a researcher present during the experiment.

3.2 Instrumentation

The application of commercially available weldable strain gauges was considered to provide local strain data on the outer housing of the surveillance test article. However before committing to the attachment of a wired, active strain gauge onto the test article, there needed to be confirmation the sensor would not be significantly affected by the electromagnetic field (EMF) of the induction heater. To test the efficacy of using a strain gauge with an induction heater, a simple experiment was conducted, shown in Figure 7, where a strain gauge (Kyowa; KHCR-5-120-G16-11) that is rated up to 750 °C and a type-K thermocouple were loosely placed in the heated zone of the test article. The induction heater was manually ramped up to approximately 700 °C by incrementally increasing the voltage and current of the induction heater. As seen in Figure 8, the signal from the type-k thermocouple was drastically impacted by the induction heating. The thermocouple instantaneously had a drop in signal from 18 °C to -250 °C when the induction heater was turned on. To observe the actual temperature of the test article, the induction heater was periodically turned off to record the real temperature readings from the thermocouple. In contrast, the strain gauge did not experience any observable drop or increase in signal when the induction heater was turned on and off. This result is promising as it provides added confidence the strain gauge is not as heavily affected from the EMF generated by the induction heating as compared to the thermocouple. However, the curved geometry and size of the test article makes it a challenge to reliably attach the weldable strain gauge onto the test article. Future work will use shielded thermocouples and will have a minimum of six thermocouples attached to the test article to quantify degree of thermal gradients present during the induction heating.

To help address the size and geometry limitations of weldable strain gauges, the DOE's NE Enabling Technologies Advanced Sensors and Instrumentation Program currently supports the development of high temperature additive manufactured strain gauges that are fabricated using direct-write printing technologies. The application of additive manufacturing allows for the fabrication of miniaturized strain sensors that can be directly fabricated onto the non-planar, curved surface of the surveillance test articles. The strain gauges have demonstrated application in moderate temperature environments up to 300 °C (Phero, 2022), however there are current efforts to increase the operating limit of the printed strain gauges for higher temperature applications (i.e., 300 °C – 950 °C). These printed strain gauges help provide valuable mechanical properties data during in-core experiments where the size and geometry of the test article limit the application of commercial weldable strain gauges. As these are developed within the Advanced Sensors and Instrumentation Program, they will be applied to this surveillance test article development and characterization.

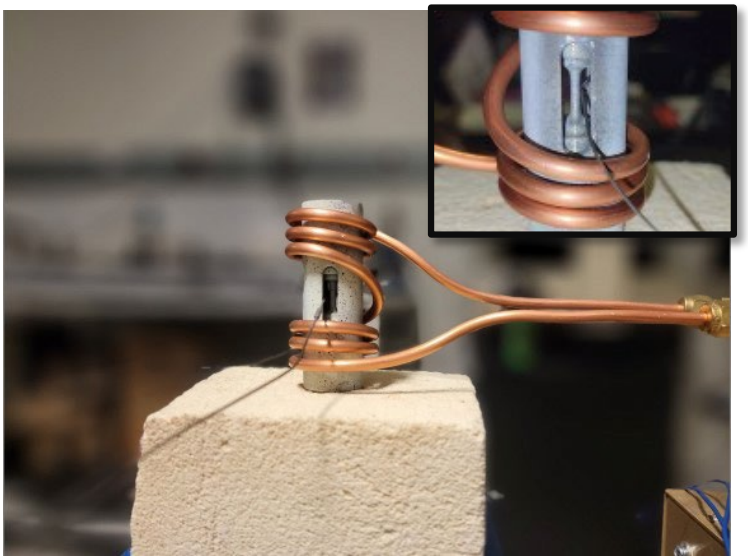

Figure 7. An unattached strain gauge and thermocouple were loosely placed in the surveillance test article on the inside of the induction heater coil to test whether the sensors are affected by the EMF generated from the heater.

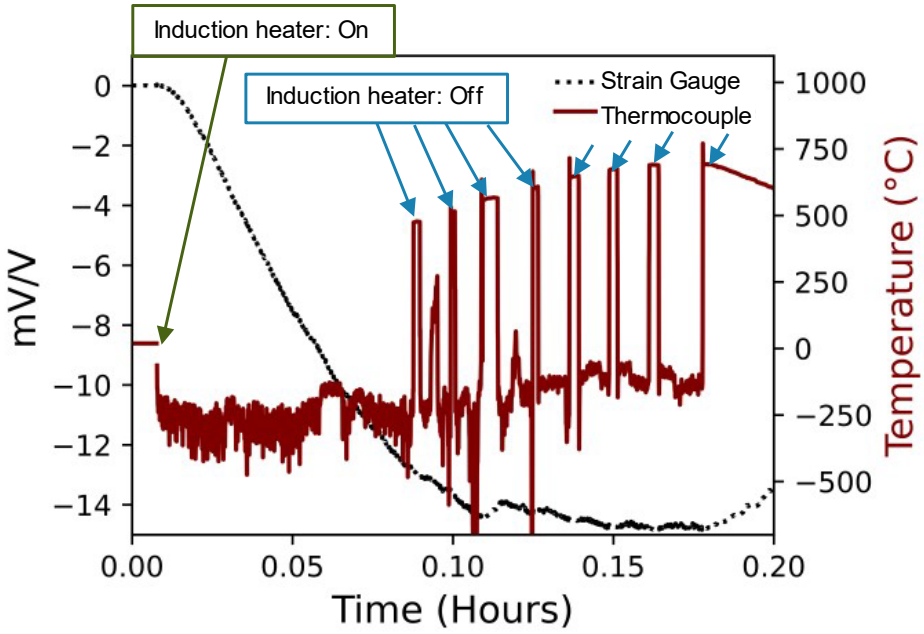

Figure 8. Raw output from the strain gauge and thermocouple during induction heating. The thermocouple was drastically affected by the induction heater, which caused the temperature to be noisy and read as a a negative value due to the strong electromagnetic field. The induction heater is periodically turned off (shown in the blue arrows) in order to read a real temperature of the surrounding environment.

3.3 Digital Image Correlation (DIC)

As the geometry of the passive surveillance test articles is complex and difficult for standard strain gauge application, instead, non-contact techniques, namely optical metrology and DIC, were determined to be suitable to assess the deformation history of the test article. The optical metrology and DIC techniques were investigated to evaluate the cycling deformation of passive test articles. Optical metrology set-up recorded the displacement of the test articles under thermal cycles using a lens-camera system, and DIC was applied for the strain analysis.

Figure 9 shows the optical metrology setup of a cylindrical passive surveillance test article. The setup includes a telescopic lens (K1-Centrimax™) attached to a forward-looking infrared camera to visualize the test article. To improve the video acquisition from the test articles, two light sources were shined onto the test article surface. As an option, a blue light filter was placed in between the test articles and the telescopic lens. All equipment was placed onto anti-vibration tables to reduce building's vibrational noise.

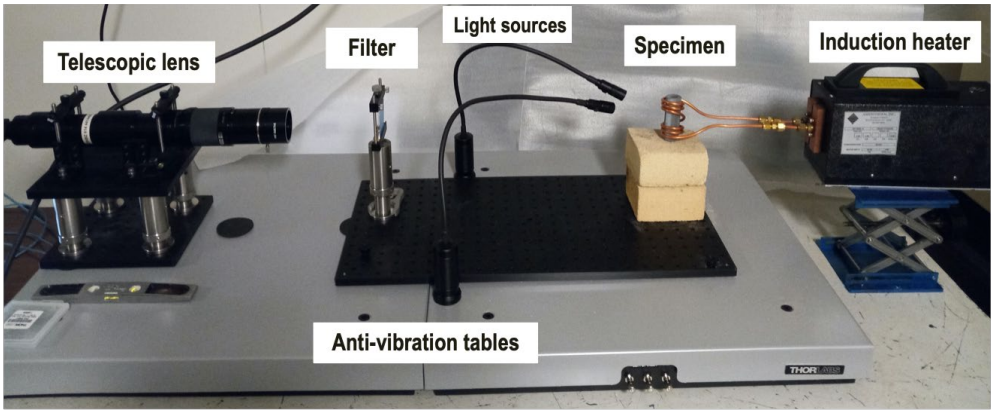

Figure 9. Optical metrology setup for the passive surveillance test article testing.

Prior to the experiments, test articles were painted using high-temperature resistant spray paints to produce a speckle pattern. A preliminary thermal cycling test was performed on the test articles with a rough speckle pattern. To improve speckle pattern quality and resolution, speckle patterns were studied on flat and cylindrical surfaces using an air brush and a graphene spray, which was shown to successfully improve the dispersion of the speckle pattern.

DIC calculations were performed using Sandia National Laboratory's Digital Image Correlation Engine (DICe) software (Turner, et. al., 2015). DICe's tracking mode was used. For tracking, two rectangular subsets were defined on the undeformed picture of the test articles. The distance between the origins of these regions formed a virtual gauge section on the test article. Displacement of these subsets was tracked during the deformation process. The engineering strain was calculated by gauge section's displacement. Complimentary DIC calculations were performed using Ncorr software as well to help validated the DICe results.

4. TEST RESULTS

4.1 DIC Assessment

The tracking mode of the DICe software was assessed on a flat dummy specimen surface that was pulled monotonically. Because a miniature specimen was used, strain gauges were not used and DIC was used to determine strain evolution. The effect of subset location, size, and shape on the strain calculations were investigated. Five subsets (P0, P1, P2, P3, and P4) were defined on the specimen surface (see Figure 10) for each effect. For each effect, the subset P0 had the largest area in pixels (px^2) among others, and it was used as the reference subset for parametrization. The percent difference between two strain values was calculated as

$$\% \, Difference = \frac{|X_1 - X_2|}{\left(\frac{X_1 + X_2}{2}\right)} \, x \, 100$$

where X1 was the reference strain from P0 and X2 was the strain calculated from the subsets 1 to 4 at the specific image frame. Percentage difference was summed over all image frames.

Figure 10 shows various subsets and the effect of subset area on the strain calculations. The gauge length and aspect ratio of the rectangles were kept constant. Corresponding areas for each subset were 36100, 22500, 12100, 4900, 900 px^2 for P0, P1, P2, P3, and P4, respectively. Areas of subsets 1-4 were normalized by dividing to the area of subset P0. The percent variation of the strain calculation was about 5% of the normalized subset area of 0.025. As the normalized subset area increase, the relative variance of the strain was sharply decreased.

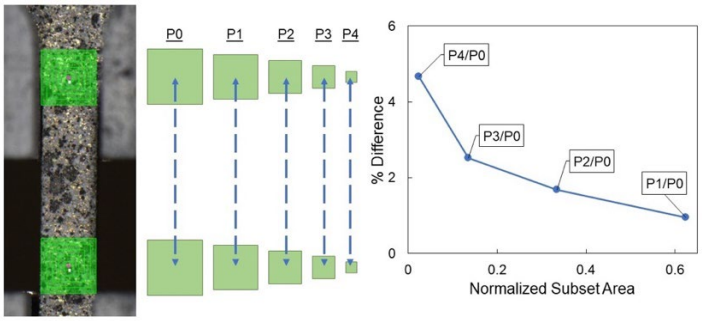

Figure 10. Rectangular subsets with changes are at the same gauge lengths and centroid locations (left) and effect of the subset area for various square subsets (right).

Figure 11 shows the subsets for the investigation of the aspect ratio and effect of the aspect ratio of rectangular subsets. The centroid of the subsets was kept same, and the width of the subset was reduced. The corresponding areas for each subset were 32300, 24700, 17100, and 9500 px^2 for the subsets from 0 to 3, respectively. Effect of the aspect ratio was minor on the strain calculations. For all subsets, the difference was below 1%.

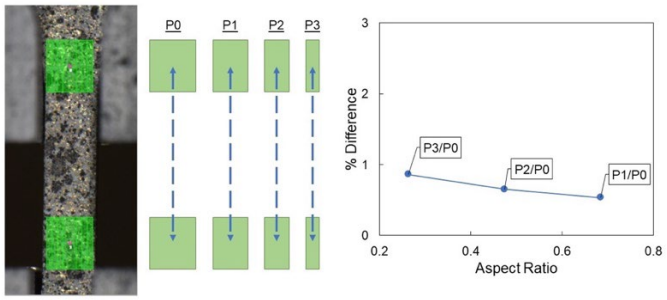

Figure 11. Rectangular subsets with changing widths at the same gauge lengths (left) and the effect of aspect ratio on the strain (right).

Figure 12 shows the impact of the gauge length on the strain measurements. The corresponding gauge lengths were 650, 570, 490, and 410 pixels for subsets of P0, P1, P2, and P3. Gauge lengths were normalized by P0 for other subsets. As the normalized gauge length reduced from 0.87 to 0.63, the percentage difference increased from ~2.5 to 7. This indicated the effect of the gauge length was significant as compared to subset area and aspect ratio.

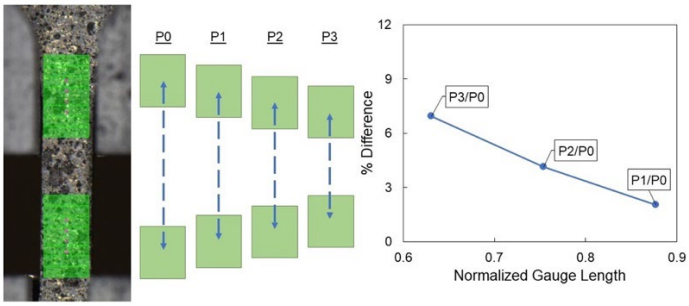

Figure 12. Rectangular subsets with different gauge length. The shape and the size of the subsets were the same, as shown on the left and the effect of the gauge length on the strain is shown on the right.

Main conclusions are that the tracking-based strain measurements allowed defining a gauge section where the strain evolution can be determined for the whole test article. Assessment of the tracking method showed that the subset selection could impact the strain measurement results. Optical metrology and DIC were able to track the specimen's deformation behavior of the passive specimen during heating and cooling. This method was applied to the preliminary testing of induction heating on the CSTA.

4.2 Preliminary Thermal Cycling Test

A preliminary thermal cycling test was performed on a CSTA that was provided by ANL. The test article was subjected to ten cycles in a nominal temperature range of 500-700°C with an average rate of 1.4 °C/s (resulting in a total cycle time of approximately 6 minutes). The deformation of the test article was analyzed by DICe's tracking mode.

Figure 13 shows the applied speckle pattern and DIC-subsets on the test article section of the passive test article at elevated temperatures of 700 and 500°C (initial cycle). The applied speckle pattern included large spots as caused by the paint-spraying process, but the pattern was sufficient to perform DIC analysis. The speckle pattern quality was intact during ten-cycle testing. Future tests will use the finer airbrushing graphene.

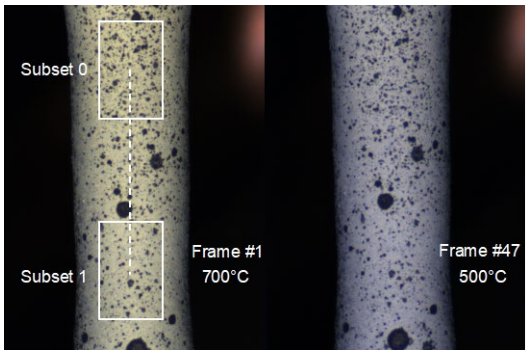

Figure 13. Image of the CSTA at different temperatures, showing DIC subsets and speckle pattern.

Figure 14 shows the evolution of the DIC-calculated strain with respect to the imposed temperature cycling. The test article was subjected to ten-cycle treatment. The speckle pattern at 700°C (the first cycle) was considered as the reference frame where the strain was set to zero. With the start of the cooling, the strain started to decrease to -1%, and it increased to 0.14%. For all cycles, the cyclic strain was captured by the DIC. For each subsequent cycle after the first, the test article was under slightly more compression, as well as reaching lower peak tension values. This test showed the potential for successfully using both induction heating paired with DIC, though it should be considered preliminary due to the uncertainties of temperature measurements and DIC calculations.

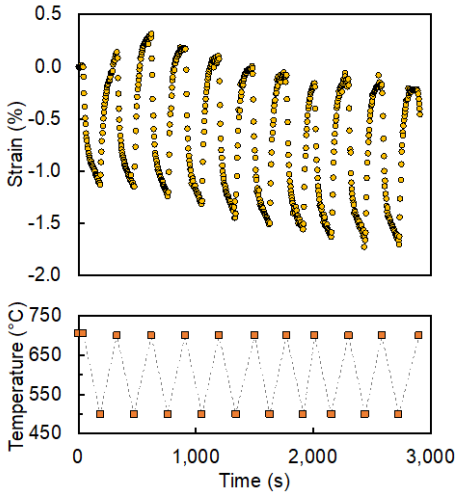

Figure 14. DIC-strain evolution during thermal cycling (ten cycles).

5. Summary and Future Work

Preliminary testing concluded that induction heating was a promising method for rapidly inducing thermal cycles within the surveillance test article. Rapid heating and cooling allowed for a full thermal cycle (700-500-700 ºC) within approximately six minutes. Strain within the gauge of the test article was tracked using DIC and matched the thermal cycles, with some apparent ratcheting occurring through the course of the cycles examined. FE modeling of the test article showed relation between the geometry of the test article, driver material, and the passive mechanical test parameters (such as elastic follow up).

For future work, shielded thermocouples will be used to better measure the temperature during the thermal cycling. Multiple thermocouples will be attached to quantify degree of thermal gradients present in the driver and test material. The automatic control system will be shortly implemented, allowing for a test article to be tested to failure (cracking, or severe ratcheting/deformation). Work will continue to

further assess tracking based DIC approach on temperature cycled test articles. The impact of the speckle pattern on the tracking DIC will be investigated as well. Potential application of printed strain gauges will also be pursued, pending development in the Advanced Sensors and Instrumentation Program. Significant work will be performed in the area of test article design. The goals of this work will be to reduce the size of the surveillance article, as well as simplify the manufacturing/welding process.

The current test article designs are still too large for deployment in operating MSRs. Efforts will continue to reduce the size and material volume of the test article.

6. REFERENCES

ASTM International. Standard Practice for Surveillance Testing of High-Temperature Nuclear Component Materials. Technical report, ASTM E531-13, 2013.

M. C. Messner, V-T. Phan, R. I. Jetter, and T-L. Sham. "Assessment of Passively Actuated In-Situ Cyclic Surveillance Test Specimens for Advanced Non-Light Water Reactors." In Pressure Vessels and Piping Conference, vol. 51593, p. V01BT01A018. American Society of Mechanical Engineers, 2018.

R. Solgi, “geneticalgorithm 1.0.2”, Programming language: Python3, United States, 2020.

M. C. Messner, Y. Momozaki, E. Boron, and T.-L. Sham, “Initial development of an in-situ, passive material surveillance test article for monitoring high temperature reactor structural components,” ANL-ART-198, Argonne National Laboratory, Lemont, IL, 2020.

M. C. Messner and T.-L. Sham, “Preliminary Procedures and Acceptance Criteria for in-situ Structural Materials Surveillance for MSR,” ANL-ART-229, Argonne National Laboratory, Lemont, IL, 2021a.

M. C. Messner, Y. Momozaki, E. Boron, G. Ye, and T.-L. Sham, “Fabrication and Testing of Two Passively Actuated Creep-Fatigue Surveillance Test Articles,” ANL-ART-228, Argonne National Laboratory, Lemont, IL, 2021.

M. C. Messner, Y. Momozaki, and E. Boron, “Report on Thermal Cycling Testing and Bimaterial Weld Development for a Passively Actuated Materials Surveillance Test Article,” ANL-ART-245, Argonne National Laboratory, Lemont, IL, 2022.

Karditsas, P.J. and Baptiste, M.J., 1995. Thermal and structural properties of fusion related materials (No. UKAEA-FUS--294). UKAEA Government Division.

Messner, M. C., and Sham, T. -L. 2021b. "Reference constitutive model for Alloy 617 and 316H stainless steel for use with the ASME Division 5 design by inelastic analysis rules". United States. https://doi.org/10.2172/1818970. https://www.osti.gov/servlets/purl/1818970.

Phero, T.L., et al., Additively manufactured strain sensors for in-pile applications. Sensors and Actuators A: Physical, 2022: p. 113691.

D. Turner, P. Crozier, P. Reu, Digital Image Correlation Engine, United States, 2015, pp. Medium: X; OS: !Mac OSX 10.9, Windows 7, Linux; Compatibility: Multiplatform.